1 Response to Editor's and Reviewers' Comments on Manuscript hess-2017-493

2 **"Effects of Micro-Arrangement of Solid Particles on PCE Migration and**

3 **Its Remediation in Porous Media**" by Ming Wu, Jianfeng Wu, Jichun Wu,

4 and Bill X. Hu

5

6 Note that the following text in Arial Narrow font denotes Editor's and Reviewers' comments and in

7 Times New Roman font denotes our response to the comments in the review. In our

8 resubmission, the marked-up manuscript version is combined in this Author's response file. All

9 changes to the original manuscript are indicated in the marked-up manuscript version. Also, in

10 our marked-up manuscript version, marked in a green strikethrough font is the text that should

11 be removed from the original manuscript and marked in a red font is the text that has been

12 added to the revision. In addition, Line number(s) mentioned below is referred to as that line

13 numbering in the marked revised manuscript.

Response to Dr. Pacheco FLA's Comments：

15 OUTLINE AND GENERAL APPRECIATION

16 This study presents the results of a contaminant transport simulation based on the migration of DNAPL

17 through an idealized porous media aquifer, which aimed to explore the control of porous media

18 microstruc-ture (micro arrangement of particles) over the migration and remediation of DNAPL at the

19 macroscopic scale. The manuscript is well organized and written. Figures and tables are of good quality

20 and are all necessary. The paper merits publication in the HESS, with a minor revision focused on issues

21 of field validation and scale. All the conceptual and mathematical frameworks are correct, but to my view

22 results cannot be extrapolated to real world conditions because no field validation is provided. Besides,

23 heterogeneity of natural aquifers largely exceeds the simulation scale (100 x 25 x 25 m). So, although the

24 effect of scale is discussed in the paper, to my view the results presented by the authors are valid solely

25 for the heterogeneity conditions generated within the simulation, which means they are not directly

26 transposed to larger field scales (see for example Pacheco, 2013 and Pacheco et al., 2015). In the

27 discussion section of the revised manuscript, the authors should explain how they think their results can

28 become representative at the aquifer scale, where heterogeneity and anisotropy are frequent, and how

29 they couple with published results for natural systems. In fact, I already reviewed various manuscripts of

30 this author and I think never saw this recommendation attended.

31 REFERENCES

32 Pacheco, F.A.L. (2013). Hydraulic diffusivity and macrodispersivity calculations imbedded in a geographic

33 information system. Hydrological Sciences Journal, v. 58, no 4, p. 930-944.

34 Pacheco, F.A.L., Landim, P.M.B., & Szocs, T. (2015). Bridging hydraulic diffusivity from aquifer to

35 particles size scale: A study on loessy sediments from SW Hungary. Hydrological Sciences Journal, v.

36 60(2), p. 269-284.

37 RECOMMENDATION Minor revision 21 September 2017 Fernando A.L. Pacheco

38 **[Response]** Comments partially accepted. We appreciate Dr. Pacheco's conscientious and

39 positive recommendation. We have made great efforts to implement the "minor revision" to

improve our manuscript as suggested. This research aims at characterizing the important effect
of micro-structure on macroscopic scale characteristics of aquifer and inner contaminant
migration and remediation. To achieve the aim of this research, the first step is to explore the
issue of theory and simulation. Fractal models of regular triangle arrangement (RTA) and
square pitch arrangement (SPA) at microscale are developed to evaluate contaminant
movement and associated contamination remediation for a synthetic heterogeneous PCE
contaminated site. Results suggest the micro arrangement of particles has obvious effects on
macroscopic PCE migration and remediation. As for the upscaling problem of the results
obtained at micro-scale, it is very important and interesting, and many previously published
studies [e.g., Pacheco et al., 2013, 2015; Dagan et al., 2013[†]; Bakshevskaia and Pozdniakov,
2016[††]] are available and worth referencing.

The upscaling problem of the results obtained at the simulation scale ($100 \times 25 \times 25$ m) is the
basic research and the upscaling problem with more complex heterogeneities needs to be
further investigated. We have made some progresses on upscaling problem from the aspects of
experiment and simulation. On this basis, we have developed the microstructure of porous
media and characterized the contaminant migration in porous media using fractal methods. So
our next step is to apply these methods to real-world aquifers with highly heterogeneous
conditions and to update our models according to general hydrogeological conditions.
Considering Dr. Pacheco's concern, we have made additional and necessary explanation of
upscaling issue in the section of Results and Discussion (lines 554-574).

Response to Referee #2's Comments：

OUTLINE AND GENERAL APPRECIATION
Anonymous Referee #2
Received and published: 16 November 2017
This paper introduced the effects of micro-structure on the contaminant migration and remediation. The
results and discussion are clearly demonstrated. This paper met the quality requirement. Language
should be proofed by peers who were native speakers. Colloquial and informal words need to be revised.
Some sentences were confused to understanding. Singular and plural problems and tense problems can
be found in this paper. Please double check format requirements of the journal and whether case of
every sentence is right
[Response] We appreciate the Referee#2's positive comments and constructive suggestions.
Accordingly, we have made great efforts to improve the manuscript and fully incorporated the

72   referee's suggestions into our revised manuscript. Moreover, we have thoroughly checked the

73   manuscript to correct English grammar errors and expression.

74   Uncertainty could be involved in real-world scenario; how did you treat the uncertainty and error in the

75   modeling?

76   **[Response]** Comments accepted. As the referee stated, uncertainty is widely existed in reality

77   and should be considered in real-world scenario. As a result, in this study, Sequential Gaussian

78   Simulation (SGS) has been used for generating 200 random realizations of heterogeneous

79   porosity field to deal with the uncertainty in the modeling.

80   Is that possible that the assumption of prorosity can be calibrated via BET analysis or other instrumental

81   methods?

82   **[Response]** Yes. This study focuses on the effect of micro-arrangement of sand particles on

83   macroscopic DNAPL migration and associated remediation for underground storage tank

84   spill. Heterogeneous porosity distribution is generated using Sequential Gaussian Simulation

85   (SGS) method. Afterwards, permeability and entry pressure are derived based on regular

86   triangle arrangement (RTA) and square pitch microscale arrangement (SPA), respectively.

87   UTCHEM is then used to simulate the entire process of DNAPL migration and remediation in

88   idealized heterogeneous contaminated site to reveal how the microstructure of porous media

89   controls the contaminant migration and remediation at macroscopic scale. BET is a common

90   technique used for determination of the surface area, porosity and other parameters of materials.

91   For realistic porous media, the porosity can be measured using BET analysis. However, this

92   issue is beyond this study and will be explored in our further work.

93   Following papers should be cited to improve this paper:

94   Shen, J., Huang, G., An, C., Zhao, S., & Rosendahl, S. (2017). Immobilization of tetrabromobisphenol A

95   by pinecone-derived biochars at solid-liquid interface: Synchrotronassisted analysis and role of inorganic

96   fertilizer ions. Chemical Engineering Journal, 321, 346-357.

97   C. J. An, E. McBean, G. H. Huang, Y. Yao, P. Zhang, X. J. Chen and Y. P. Li. (2016). Multi-Soil-Layering

98   Systems for Wastewater Treatment in Small and Remote Communities. Journal of Environmental

99   Informatics, 27(2), 131-144.

100   A. K. Mishra, B. Kumar and J. Dutta. (2016). Prediction of Hydraulic Conductivity of Soil Bentonite

101   Mixture Using Hybrid-ANN Approach. Journal of Environmental Informatics, 27(2), 98-105.

102   Interactive comment on Hydrol. Earth Syst. Sci. Discuss., https://doi.org/10.5194/hess-2017-

103   493, 2017.

104   **[Response]** Comments accepted and the references have been cited in the revised manuscript.

105   We are grateful to the referee's whose constructive suggestions have led to significant

106   improvement of the manuscript.

Effects of Micro-Arrangement of Solid Particles on PCE Migration and Its Remediation in Porous Media

Ming Wu[1,2], Jianfeng Wu [1*], Jichun Wu[1**], and Bill X. Hu[2]

[1]Key Laboratory of Surficial Geochemistry, Ministry of Education; Department of

Hydrosciences, School of Earth Sciences and Engineering, Nanjing University, Nanjing

210023, China

[2]Institute of Groundwater and Earth Sciences, Jinan University, Guangzhou 510632, China

Correspondence to: J.F. Wu (jfwu@nju.edu.cn), J. C. Wu (jcwu@nju.edu.cn)

125

ABSTRACT

Groundwater can be stored abundantly in granula-composed aquifers with high permeability. The micro-structure of granular materials has important effect on ~~aquifer~~ the permeability of aquifers; and the contaminant migration and remediation in aquifers is also influenced by the characteristics of porous media. In this study, two different microscale arrangements of sand particles are ~~examined~~ compared to reveal the effects of micro-structure on the contaminant migration and remediation. With the help of fractal theory, the mathematical expressions of permeability and entry pressure are conducted to delineate granular materials with regular triangle arrangement (RTA) and square pitch arrangement (SPA) at microscale. Using Sequential Gaussian Simulation (SGS) method, a synthetic heterogeneous site contaminated by Perchloroethylene (PCE) is then used to investigate the migration and remediation affected by the two different micro-scale arrangements. PCE is released from an underground storage tank into the aquifer and the surfactant is used to clean up the subsurface ~~environment~~contamination. Results suggest that RTA can not only ~~can~~ cause larger range of groundwater contamination, but also ~~can cause harder~~ make remediation become more difficult ~~for contaminated aquifer~~. The PCE remediation efficiency of 60.01% -99.78% with a mean of 92.52% and 65.53% -99.74% with a mean of 95.83% are achieved for 200 individual heterogeneous realizations based on the RTA and SPA, respectively, indicating that the cleanup of PCE in aquifer with SPA is significantly easier. This study leads to a new understanding of the microstructures of porous media and demonstrates how micro-scale arrangements control contaminant migration in aquifers, which is helpful to design successful remediation scheme for underground storage

147   tank spill.

148   **Keywords:** microscale arrangement; regular triangle; square pitch; contaminant migration and

149   remediation; cumulative PCE removal; macroscopic scale

150

1. Introduction

152   Groundwater is an essential natural resource for water supply to domestic, agricultural,

153   industrial activities and ecosystem health (Boswinkel, 2000; Valipour, 2012; Valipour, 2015;

154   Yannopoulos et al., 2015; Valipour and Singh, 2016). Unfortunately, with the rapid

155   development of economic activities such as mining, agriculture, landfills and industrial

156   activities (Bakshevskaia and Pozdniakov, 2016; Cui et al., 2016; Liu et al., 2016; An et al.,

157   2017; Shen et al., 2017), more and more contaminants released from human activities are

158   contaminating the precious groundwater resource and subsurface environment (Dawson and

159   Roberts, 1997; Liu, 2005; Hadley and Newell, 2014; C.Carroll et al., 2015; Essaid et al., 2015;

160   Huang et al., 2015; Liu et al., 2016; Schaefer et al., 2016; Weathers et al., 2016). ~~Out of~~Among

161   the contaminants detected in groundwater, dense nonaqueous phase liquids (DNAPLs) such

162   as perchloroethylene (PCE) and other polycyclic aromatic hydrocarbons (PAHs), are highly

163   toxic and carcinogenic (Dawson and Roberts, 1997; Hadley and Newell, 2014). When

164   DNAPLs are released into aquifer from underground storage tank, they will infiltrate through

165   the entire aquifer and form residual ganglia and pools of DNAPLs due to their large densities,

166   high interfacial tension, and low solubility. The residual ganglia and pools of DNAPLs can

167   serve as long-term sources of groundwater contamination ~~that~~ which are~~is~~ harmful to

168   subsurface environment and human beings (Bob et al., 2008; Liang and Lai, 2008; Liang and

169 Hsieh, 2015). Consequently, it is very important to explore DNAPL migration in aquifer and

170 ~~mitigate~~ associated remediation of groundwater contamination ~~by appropriate remediation~~.

171   When DNAPLs migrate~~s~~ in aquifers at macroscopic scale, the transport properties

172 such as permeability, diffusivity and dispersivity are closely related to the aquifer's

173 microstructures and can affect DNAPLs behavior (Yu and Li, 2004; Yu, 2005; Yun et al.,

174 2005; Feng and Yu, 2007; Yu et al., 2009). Therefore, characterizing the effect of

175 microstructures on macroscopic properties is a key point of research on heterogeneity of

176 porous media (Mishra et al., 2016). In the classical Kozeny–Carman equation, the

177 permeability K is related to porosity n, surface area S and the Kozeny constant c , where c is

178 affected by the porosity, solid particles and micro geometric structures (Bear 1972; Yu et al.

179 2009). According to fractal theory, natural porous media can be treated as fractal objects

180 (Pfeifer and Avnir 1983; Katz and Thompson 1985; Krohn 1988). For example, the tortuosity

181 of flow path in porous media is deeply studied by various proposed fractal models (Yu and

182 Cheng 2002; Yu et al. 2009; Cai et al. 2010), indicating the effectiveness of fractal methods

183 ~~compared to experimental observations~~. Based on fractal concepts, mathematic models are

184 proposed to depict the permeability and invasion of fluids in some special porous media (Yu

185 and Cheng 2002; Yu et al. 2009; Cai et al. 2010). Furthermore, fractal method is also used to

186 explore the effect of microstructure of biological media on associated thermal conductivity

187 while this kind of material has a complex randomly distributed vascular trees structure at

188 microscale (Li and Yu 2013).

189 In this study, we focus on the effect of micro-arrangement of sand particles on macroscopic

190 DNAPL migration and associated remediation for underground storage tank spill. With the

191   help of fractal theory, the microstructures of two different microscale arrangements of sand

192   particles are explored. Afterwards, the mathematical relationships between porosity and

193   permeability, entry pressure are derived for regular triangle arrangement (RTA) and square

194   pitch microscale arrangement (SPA). Idealized heterogeneous contaminated site is generated

195   using Sequential Gaussian Simulation (SGS) method. Underground storage tank releases PCE

196   into heterogeneous aquifer composed of granular material ~~and migrates freely~~. After long time

197   migration, PCE contamination is alleviated using surfactant remediation method. A

198   multicomponent, multiphase model simulator UTCHEM is then used to simulate the entire

199   process of DNAPL migration and remediation. Effects of arrangements of sand particles on

200   migration and remediation of DNAPLs are comparatively analyzed based on the simulations to

201   reveal how the microstructure of porous media controls the contaminant migration and

202   remediation at macroscopic scale.

203   **2. Methodology**

204   **2.1 Fractal models of two different microscale arrangements of sand particles**

205   The porous media can be treated as the bundle of tortuous capillary tubes, the

206   relationship between the diameter and the length of capillary tube are (Yu and Cheng, 2002):

207    $$L_t(\lambda) = \lambda^{1-D_t} L_s^{D_t} \tag{1}$$

208   where L_s is the straight length between the tortuous flow path's end point; λ is the diameter

209   of capillary tube; D_t is the fractal dimension of tortuosity for porous media, $1<D_t<2$ (Yu and

210   Cheng, 2002).

211   Select an infinitesimal element consisting of a bundle of tortuous capillary tubes form

212 porous media, the total number of capillary tubes in infinitesimal element can be calculated

213 by the power-law relation:

214
$$N(L \geq \lambda) = (\frac{\lambda_{max}}{\lambda})^{D_f}$$
(2)

215 where D_f is the fractal dimension for pore areas in porous media, $1 < D_f < 2$ (Yu and Cheng,

216 2002); λ_{max} is the maximum diameter of capillary tubes.

217   Afterward, the derivative of Equation (2) can be achieved:

218
$$-dN(L \geq \lambda) = D_f \lambda_{max}^{D_f} \lambda^{-(D_f+1)} d_\lambda$$
(3)

219   The total number of capillary tubes in infinitesimal element can be derived from

220 Equation (3):

221
$$N_t(L \geq \lambda_{min}) = (\frac{\lambda_{max}}{\lambda_{min}})^{D_f}$$
(4)

222 where λ_{min} is the minimum diameter of capillary tubes.

223   Dividing Equation (3) by Equation (4) can achieve:

224
$$-\frac{d_{N(L \geq \lambda)}}{N_t} = D_f \lambda_{min}^{D_f} \lambda^{-(D_f+1)} d_\lambda = f(\lambda) d_\lambda$$
(5)

225 where $f(\lambda)$ is the probability density function, $f(\lambda) = D_f \lambda_{min}^{D_f} \lambda^{-(D_f+1)}$ ~~., it should satisfy~~

226 $\int_{-\infty}^{+\infty} f(\lambda) d_\lambda = 1 - (\frac{\lambda_{min}}{\lambda_{max}})^{D_f}$ ~~.If~~ $(\frac{\lambda_{min}}{\lambda_{max}})^{D_f} = 0$ ~~-~~

227   The probability density function satisfies the relationship:

228
$$\int_{-\infty}^{+\infty} f(\lambda) d_\lambda = 1 - (\frac{\lambda_{min}}{\lambda_{max}})^{D_f}$$
(6)

229   Considering $(\frac{\lambda_{min}}{\lambda_{max}})^{D_f} = 0$, the above Equation (6) becomes:

230
$$\int_{-\infty}^{+\infty} f(\lambda) d_\lambda = \int_{\lambda_{min}}^{\lambda_{max}} f(\lambda) d_\lambda = 1 - (\frac{\lambda_{min}}{\lambda_{max}})^{D_f} = 1$$
(7)

231   When fluid flow in capillary tubes, the flow rate Q can be calculated by the

232   Hagen–Poiseulle equation:

$$Q = \frac{\pi r^4 \Delta P}{8\mu L_s} = \frac{\pi (\frac{\lambda}{2})^4 \Delta P}{8\mu L_s} = \frac{\pi \lambda^4 \Delta P}{128 \mu L_s} \tag{8}$$

234   where μ is fluid's viscosity; ΔP is the pressure gradient across the capillary tube.

235   The differentiation of flow rate of capillary tubes is (Yu and Cheng, 2002):

$$
\begin{aligned}
d_q &= [-d_{N(L \geq \lambda)}] \frac{\pi \lambda^4 \Delta P}{128 \mu L_t(\lambda)} = D_f \lambda_{max}^{D_f} \lambda^{-(D_f+1)} d_\lambda \cdot \frac{\pi \lambda^4 \Delta P}{128 \mu L_t(\lambda)} \\
&= \frac{\pi}{128} \frac{\Delta P}{\mu} \frac{D_f \lambda_{max}^{D_f}}{L_t(\lambda)} \lambda^{3-D_f} d_\lambda = \frac{\pi}{128} \frac{\Delta P}{\mu} \frac{D_f \lambda_{max}^{D_f}}{\lambda^{1-D_t} L_s^{D_t}} \lambda^{3-D_f} d_\lambda \\
&= \frac{\pi}{128} \frac{\Delta P}{\mu} \frac{D_f \lambda_{max}^{D_f}}{L_s^{D_t}} \lambda^{2+D_t-D_f} d_\lambda
\end{aligned}
\tag{9}
$$

237   Integrating the individual flow rate from λ_{min} to λ_{max} can achieve the total flow rate (Yu

238   and Cheng, 2002):

$$
\begin{aligned}
Q &= \int d_q = \int_{\lambda_{min}}^{\lambda_{max}} \frac{\pi}{128} \frac{\Delta P}{\mu} \frac{D_f \lambda_{max}^{D_f}}{L_s^{D_t}} \lambda^{2+D_t-D_f} d_\lambda \\
&= \frac{\pi}{128} \frac{\Delta P}{\mu} \frac{D_f}{3-D_f+D_t} \frac{1}{L_s^{D_T}} \lambda_{max}^{D_f} (\lambda_{max}^{3-D_f+D_t} - \lambda_{min}^{3-D_f+D_t}) \\
&= \frac{\pi}{128} \frac{\Delta P}{\mu} \frac{D_f}{3-D_f+D_T} \frac{1}{L_s^{D_t}} \lambda_{max}^{3+D_t} [1 - (\frac{\lambda_{min}}{\lambda_{max}})^{D_f} (\frac{\lambda_{min}}{\lambda_{max}})^{3+D_t-2D_f}]
\end{aligned}
\tag{10}
$$

240   Due to $1<D_t<2$ and $1<D_f<2$, then $3+D_T-2D_f>0$. Simultaneously, $(\frac{\lambda_{min}}{\lambda_{max}})^{D_f} \cong 0$,

241    $0 < (\frac{\lambda_{min}}{\lambda_{max}})^{3+D_T-D_f} < 1$. Therefore, Equation (10) can be simplified as:

$$Q = \int d_q = \frac{\pi}{128} \frac{\Delta P}{\mu} \frac{D_f}{3-D_f+D_T} \frac{1}{L_0^{D_T}} \lambda_{max}^{3+D_T} \tag{11}$$

243   Substituting Darcy's law $Q = \frac{kA\Delta P}{\mu L_0}$ in Equation (11) will obtain the permeability of

244   porous media:

$$k = \frac{\pi}{128} \frac{D_f}{3 + D_T - D_f} \frac{L_0^{1-D_T}}{A} \lambda_{\max}^{3+D_T} \qquad (12)$$

245

246   To obtain the fractal dimension of tortuosity D_t, the expression of tortuosity (τ) can be

247   obtained from Equation (1):

$$\tau = \frac{L_t(\lambda)}{L_s} = \frac{\lambda^{1-D_t} L_s^{D_t}}{L_s} = (\frac{L_s}{\lambda})^{D_t - 1} \qquad (13)$$

248

249   Then ~~the~~ $D_t$$D_f$ is given by (Yu and Li, 2001):

$$D_{\mathrm{t}} = 1 + \frac{\ln \tau}{\ln(\dfrac{L_s}{\lambda})} \qquad (14)$$

250

251   RTA and SPA are shown in Fig. 1. An equilateral triangle and a square are selected

252   from the two micro-structures as unit cells (Fig. 1a and Fig. 1b). The unit cell of equilateral

253   triangle is composed of three solid particles and the pore among them, while the unit cell of

254   square is composed of four solid particles. For the unit cell of RTA in Fig. 1a, corresponding

255   porosity is given by:

$$n = \frac{A_a - \pi R_v^2 / 2}{A_a} \qquad (15)$$

256

257   where n is porosity; A_a is the total area of equilateral triangle; R_v is the average radius of

258   solid particles. The total area of equilateral triangle can be achieved:

$$A_a = \frac{\pi R_v^2}{2(1-n)} \qquad (16)$$

259

260   The side length of the equilateral triangle in Fig. 1a can be calculated as:

$$L_a = R_v \sqrt{\frac{2\pi}{\sqrt{3}(1-n)}} \qquad (17)$$

261

262   where L_a is the side length.

263   The area of irregular pore among solid particles is given by:

$$A_{ap} = A_a - \frac{\pi R_v^2}{2} = \frac{\pi R_v^2 n}{2(1-n)} \qquad (18)$$

265   where A_{ap} is the area of pore in the unit cell.

266   Approximate the pore in the equilateral triangle as a circle, then the maximum

267   diameter of pore can be obtained:

$$\lambda_{max,a} = R_v \sqrt{\frac{2n}{1-n}} \qquad (19)$$

269   where $\lambda_{max,a}$ is the diameter of capillary tube in equilateral triangle. The fluid <u>does not</u>

270   pass<s>es not only</s> the central-pore of the unit cell, but also <u>flow through</u> the gap between

271   adjacent particles. The gap length and the average diameter of capillary tube perpendicular

272   to the plane of equilateral triangle are calculated as follows:

$$\Delta L_a = L_a - 2R_v = R_v \left(\sqrt{\frac{2\pi}{\sqrt{3}(1-n)}} - 2 \right) \qquad (20)$$

$$\lambda_a = \frac{\lambda_{max,a} + \Delta L_a}{2} = \frac{R_v}{2} \left(\sqrt{\frac{2n}{1-n}} + \sqrt{\frac{2\pi}{\sqrt{3}(1-n)}} - 2 \right) \qquad (21)$$

275   where ΔL_a is the gap length between solid particles; λ_a is the average diameter of capillary

276   tubes in the equilateral triangle.

277   Generally, the tortuosity of flow path in porous media is the ratio of the length of tortuous

278   flow path to the straight length of flow path along the flow direction (Taiwo et al., 2016):

$$\tau = \frac{L_t}{L_s} \qquad (22)$$

280   where L_t is the length of tortuous flow path; and L_s is the straight length of flow path along the

281   flow direction.

282   For the flow path shown in Fig. 1a, the L_t and L_s respectively are:

$$L_t = (h_o - R_v) + \frac{\pi R_v}{2} = R_v \left(\sqrt{\frac{\sqrt{3}\pi}{2(1-n)}} + \frac{\pi}{2} - 1 \right) \qquad (23)$$

$$284 \qquad\qquad L_s = h_o = R_v \sqrt{\frac{\sqrt{3}\pi}{2(1-n)}} \qquad\qquad (24)$$

285   where h_o is the altitude of the equilateral triangle, $h_o = \dfrac{\sqrt{3}}{2} L_a = R_v \sqrt{\dfrac{\sqrt{3}\pi}{2(1-n)}}$.

286   Consequently, the tortuosity of RTA is yielded:

$$287 \qquad\qquad \tau = \frac{L_t}{L_s} = 1 + \frac{\dfrac{\pi}{2}-1}{\sqrt{\dfrac{\sqrt{3}\pi}{2(1-n)}}} \qquad\qquad (25)$$

288   The D_f is determined using Sierpinkski gasket (Fig. 2) in fractal theory (Yu and Cheng,

289   2002). The shaded area represents solid of porous media and the white area represents pore.

290   The pore area fractal dimension in Figs. 2a-c are 0.000, 1.000 and 1.594, respectively

291   ($1 = L_a^{D_f} = 2^{D_f}$, $3 = L_a^{D_f} = 3^{D_f}$, $13 = L_a^{D_f} = 5^{D_f}$). Based on the Sierpinkski gasket, the

292   dimensionless pore area in RTA (Fig. 1a) is approximated as:

$$293 \qquad\qquad A_{apd} = (L_a^+)^{D_f} \qquad\qquad (26)$$

294   where A_{apd} is the dimensionless pore area of RTA; $L_a^+ = L_a / \lambda_{min}$. Equation (26) can be

295   solved to achieve D_f:

$$296 \qquad\qquad D_f = \frac{\ln A_{apd}}{\ln L_a^+} \qquad\qquad (27)$$

297   The porosity equals to the ratio of the dimensionless pore area of RTA (A_{apd}) to the

298   dimensionless total area of RTA (A_a^+):

$$299 \qquad\qquad n = \frac{A_{apd}}{A_a^+} \qquad\qquad (28)$$

300   where $A_a^+ = \dfrac{A_a}{\pi\lambda_{min}^2/4} = \dfrac{\dfrac{\pi R_v^2}{2(1-n)}}{\pi\dfrac{\lambda_{min}^2}{4}} = \dfrac{2R_v^2}{\lambda_{min}^2}\dfrac{1}{1-n} = \dfrac{(d^+)^2}{2}\dfrac{1}{1-n}$; $d^+ = \dfrac{2R_v}{\lambda_{min}}$, $L_a^+ = \sqrt{A_a^+}$.

From Equation (28), the dimensionless pore area of RTA (A_{apd}) is given by:

$$A_{apd} = n \cdot A_a^+ \tag{29}$$

The dimensionless total area of RTA (A_a^+) can be written as:

$$A_a^+ = (L_a^+)^2 \tag{30}$$

Afterward, L_a^+ is calculated as:

$$L_a^+ = \sqrt{A_a^+} = \sqrt{\frac{(d^+)^2}{2} \frac{1}{1-n}} = d^+ \sqrt{\frac{1}{2(1-n)}} \tag{31}$$

Substituting Equation (29) and Equation (31) into Equation (27) will derive D_f of RTA:

$$D_f = \frac{\ln A_{apd}}{\ln L_a^+} = \frac{\ln(n \cdot A_a^+)}{\ln(\sqrt{A_a^+})} = 2 + \frac{\ln(n)}{\ln(\sqrt{A_a^+})} = 2 + \frac{\ln(n)}{\ln(d^+ \sqrt{\frac{1}{2(1-n)}})} \tag{32}$$

For the unit cell of square shown in Fig. 1b, the porosity is:

$$n = \frac{A_b - \pi R_v^2}{A_b} \tag{33}$$

where A_b is the total area of the square. Equation (33) can also be expressed as the area of

unit cell:

$$A_b = \frac{\pi R_v^2}{1-n} \tag{34}$$

Again, the side length of the square is:

$$L_b = \sqrt{A_b} = R_v \sqrt{\frac{\pi}{1-n}} \tag{35}$$

Consequently, the area of irregular pore in the square is given by:

$$A_{bp} = A_b - \pi R_v^2 = \frac{n \pi R_v^2}{1-n} \tag{36}$$

where A_{bp} is the area of pore in the square.

Approximate the pore as a circle and obtain corresponding maximum diameter:

$$\lambda_{max,b} = 2R_v \sqrt{\frac{n}{1-n}} \tag{37}$$

320

321 where $\lambda_{max,b}$ is the maximum diameter of capillary tube perpendicular to the plane of the

322 square. Similarly, fluid flows through the central-pore in the square and the gap between

323 adjacent particles. As a result, the gap and average diameter of capillary tube are expressed

324 as:

$$\Delta L_b = L_b - 2R_v = R_v \left(\sqrt{\frac{\pi}{1-n}} - 2 \right) \tag{38}$$

325

$$\lambda_b = \frac{\lambda_{max,b} + \Delta L_b}{2} = \frac{R_v}{2} \left(2\sqrt{\frac{n}{1-n}} + \sqrt{\frac{\pi}{1-n}} - 2 \right) \tag{39}$$

326

327 where ΔL_b is the gap length between the adjacent two solid particles; λ_b is the average

328 diameter of capillary tube.

329 For the tortuous flow path in Fig. 1b, the L_t and L_s respectively are given by:

$$L_t = \Delta L_b + \pi R_v = R_v \left(\sqrt{\frac{\pi}{1-n}} - 2 + \pi \right) \tag{40}$$

330

$$L_s = L_b = R_v \sqrt{\frac{\pi}{1-n}} \tag{41}$$

331

332 Afterward, the tortuosity of SPA yields:

$$\tau = \frac{L_t}{L_s} = 1 + \frac{\pi - 2}{\sqrt{\frac{\pi}{1-n}}} \tag{42}$$

333

334 The procedure of deriving D_f of SPA is similar to the procedure of calculating D_f of RTA.

335 Similarly, the D_f and porosity of SPA (Fig. 1b) are given by:

$$D_f = \frac{\ln A_{bpd}}{\ln L_b^+} \tag{43}$$

336

$$n = \frac{A_{bpd}}{A_b^+} \tag{44}$$

337

where A_{bpd} is the dimensionless pore area of SPA; $L_b^+ = L_b / \lambda_{min}$, A_b^+ is the dimensionless

total area of SPA, $A_b^+ = \dfrac{A_b}{\pi \lambda_{min}^2 / 4} = \dfrac{\dfrac{\pi R_v^2}{1-n}}{\pi \dfrac{\lambda_{min}^2}{4}} = \dfrac{4R_v^2}{\lambda_{min}^2} \dfrac{1}{1-n} = (d^+)^2 \dfrac{1}{1-n}$.

The dimensionless pore area of SPA (A_{bpd}) can be yielded from Equation (44):

$$A_{bpd} = n \cdot A_b^+ \qquad (45)$$

L_b^+ can be calculated as:

$$L_b^+ = \sqrt{A_b^+} = \sqrt{(d^+)^2 \dfrac{1}{1-n}} = d^+ \sqrt{\dfrac{1}{1-n}} \qquad (46)$$

Substituting Equation (45) and Equation (46) into Equation (43), $-D_f$ of SPA can be

derived:

$$D_f = \dfrac{\ln A_{bpd}}{\ln L_b^+} = \dfrac{\ln(n \cdot A_b^+)}{\ln(\sqrt{A_b^+})} = 2 + \dfrac{\ln(n)}{\ln(\sqrt{A_b^+})} = 2 + \dfrac{\ln(n)}{\ln(d^+ \sqrt{\dfrac{1}{1-n}})} \qquad (47)$$

The entry pressure of tortuous capillary tube (P_c) is defined by Young-Laplace

equation as follows (Ahn and Seferis, 1991):

$$P_c = \dfrac{\omega}{\lambda} \dfrac{1-n}{n} \qquad (48)$$

where P_c is the entry pressure; λ is the diameter of capillary tube; ω equals to $F\sigma\cos\theta$ in

which θ is the contact angle between fluid and solid, σ is the surface tension of the wetting

fluid, and F is the form factor depending on the capillary tube alignment and the flow

direction.

2.2 Dealing with the heterogeneity of porous media

In this study, Sequential Gaussian Simulation (SGS) is used to generate random

realization of heterogeneous porosity field. SGS is a stochastic simulation method combining

357 sequential principle and Gaussian method. It assumes variable fit to Gaussian random field.

358 The gauss distribution function is constructed at the each simulated spatial location based on

359 the characteristics of variation function, afterward, randomly selects a value as the variable at

360 the location. In SGS method, observation data are transformed to Gaussian distribution or

361 normal distribution. Based on current sample data, the conditional probability distribution of

362 points to be simulated is calculated by SGS method and then simulation is performed based on

363 semivariogram model. Each simulated value, together with measured data and previous

364 simulation data, becomes the conditional data set for the next step. As simulation proceeds, the

365 conditional data set increases. Pervious researches suggested 50–400 realizations are required

366 to obtain a statistically stable mean realization (Eggleston et al., 1996; Hu et al., 2007).

2.3 Modeling PCE migration and its remediation

368 The DNAPL migration and remediation are modeled using a multi-component,

369 multi-phase, and multi-composition of contaminant transport processes simulator named

370 UTCHEM (University of Texas Chemical Compositional Simulator) (Delshad et al., 1996). As

371 an extension to Delshad's work, UTCHEM was developed by University of Texas as a

372 comprehensive and practical tool. In numerous applications, UTCHEM has proved to be

373 particularly useful in simulation of contaminant migrations and has been a popular multi-phase

374 flow and, multi-constituent, reactive transport model used widely in groundwater simulations.

375 UTCHEM account for chemical, physical and biological reactions, complex non-equilibrium

376 sorption, decay and geochemical reactions and, surfactant-enhanced solubilization and

377 mobilization of DNAPLs., mMoreover, heterogeneous properties of porous media is also

378 consideredaddressed. As a result, UTCHEM has been adapted for a variety of environmental

379   applications such as surfactant-enhanced aquifer remediation (SEAR). In this study, DNAPL

380   migration and remediation for cleaning up DNAPL contamination in idealized heterogeneous

381   site are simulated by UTCHEM.

3. Application to a synthetic heterogeneous PCE contaminated site

382

3.1 Site description

383

384   The idealized domain synthetic application is a two-dimensional confined aquifer

385   ~~saturated by water~~ (Fig. 3). The length, width and depth of aquifer are 101 m, 25 m and 25 m,

386   respectively. Idealized aquifer is discretized into 101 grids horizontally and 25 layers

387   vertically (Fig. 3b). The spacing of each grid is uniformly 1 m along x and z directions, and

388   the longitudinal and transverse dispersivities are set as to 1.0 m and 0.1 m, respectively.

389   Horizontal and vertical correlation length values is 5 m. The top and bottom borders of aquifer

390   are defined as no-flow boundaries, while the left and right borders are defined as constant

391   potential boundaries to create a groundwater flow from left to right under a low hydraulic

392   gradient of 0.005 m/m (Liu et al., 2003; Liu, 2005; Qin et al., 2007). The porous media of

393   idealized aquifer is assumed to be heterogeneous and mixed by different grades of sands.

394   The porosity of aquifer is assumed spatially and uniformly distributed with average value

395   of 0.220 and standard deviation of 0.060. In this study, porosity follows normal distribution

396   and its standard deviation (SD) represents the enhanced geological heterogeneity. 200

397   realizations porosity field are generated using Sequential Gaussian Simulation (SGS). One of

398   the 200 realizations of heterogeneous field is shown in Fig. 4a. Simultaneously, statistical

399   assessment is taken on the individual realization of porosity field and corresponding

400   histograms are shown in Fig. 4b. We can find the frequency of the individual realization of

401   porosity field is close to normal distribution, which conform to the ~~fact~~ situation that most

402   characteristic of natural aquifer can be expressed as normal distribution (Montgomery et al,

403   1987). Based on the heterogeneous porosity field, the fractal dimension of tortuosity D_t, the

404   fractal dimension for pore areas D_f and the diameter of capillary tube in porous media,

405   permeability is obtained by the Equation (12). Fig. 4c shows the individual heterogeneous

406   permeability field selected from the 200 realizations of RTA, besides, the result of associated

407   frequency analysis is shown in Fig. 4d. The permeability field fits the lognormal distribution

408   obviously, which has been presented by many researches that the parameter of aquifer

409   penetrability ~~is~~ follows lognormal distribution ~~field~~ (Montgomery et al., 1987; Veneziano and

410   Tabaei, 2004). Compared to histogram of porosity field in Fig. 4b, the shape of permeability is

411   similar. The individual heterogeneous permeability field of SPA is shown in Fig. 4e.

412   Corresponding frequency analysis of SPA reveals the permeability field is lognormal

413   distribution, while some difference appears compared with RTA (Fig. 4f). The average

414   permeability of individual realization of RTA is 2.012×10^{-12} m^2 and the average permeability of

415   individual realization of SPA is 1.618×10^{-12} m^2. For 200 realizations, the average permeability

416   of RTA and SPA are 2.120×10^{-12} m^2 and 1.706×10^{-12} m^2, indicating the permeability of RTA is

417   bigger than SPA slightly.

418   The average pore diameters of two different microscale arrangements of particles are

419   derived using corresponding fractal models. In detail, average diameter of RTA is calculated

420   by Equation (21) and average diameter of SPA is calculated by Equation (39). Consequently,

421   the entry pressure of the two kinds of microscale arrangements can be obtained by Equation

422 (48), respectively. The individual entry pressure fields of two microscale arrangements and

423 associated frequency analysis are shown in Figs. 4g-j. From the frequency of entry pressure in

424 Fig. 4h and Fig. 4j, the entry pressures of both RTA and SPA are the lognormal distributions.

425 However, the average entry pressure of individual realization of RTA is 1.980 kPa, while the

426 average entry pressure of SPA is 1.481 kPa. For 200 realizations of entry pressure field, the

427 average entry pressure of RTA is 1.922 kPa and the average entry pressure of SPA is 1.442 kPa.

428 The differences of average entry pressure ~~and the entry pressure distributed range~~ between RTA

429 and SPA imply the micro-structure of aquifer has effect on the macroscopic characteristics.

430   The purpose of this study is to explore the effects of micro-structure of aquifer on DNAPL

431 migration and remediation. A PCE spill event (the leaking of underground storage tank) occurs

432 on the top of the aquifer and a surfactant remediation is ~~desired~~designed to clean up the

433 contaminated aquifer. The total duration of 300 days is divided into four stages: (1) 300 m^3

434 PCE is released from underground storage tank into aquifer at the top layer of spill position

435 shown in Fig. 3a during 0~30 days; (2) PCE migrates in aquifer freely during 30~100 days; (3)

436 surfactant is injected into aquifer during 100~150 days; and (4) water flushing during 150~300

437 days. In the first stage, PCE is released as a point pollution source in the center grid block at

438 the top layer of the aquifer, which spill is at a constant rate of 10 m^3/day. After PCE coming

439 into heterogeneous aquifer, PCE is migrating freely under the effects of gravity and the natural

440 hydraulic gradient condition. The PCE not only migrates downward through the aquifer, but

441 also can be trapped by capillary forces as residual ganglia and globules. During the long-term

442 PCE migration period, PCE is contaminating groundwater and expanding plume. To clean up

443 the contaminated aquifer, 4% surfactant solution is injected into aquifer through the two

444 injection wells (Fig. 3b) at a constant rate of 80 m^3/day, simultaneously, contaminated

445 groundwater is extracted through production well at constant rate of 160 m^3/day.   Surfactant

446 can reduce the interfacial tension between DNAPL and aqueous phase to promote

447 solubilization and mobilization of DNAPL in aquifer. After surfactant injection, the

448 contaminated aquifer is flushed by water over a long time of 150 days. Based on the

449 distributions of porosity, permeability and entry pressure of two microscale arrangements, the

450 entire PCE migration and remediation process is simulated by a multicomponent, multiphase

451 model simulator UTCHEM (Delshad et al., 1996). The parameters used in simulation are listed

452 in Table 1. Simulation results of two different microscale arrangements are compared to reveal

453 the effect of microstructure on the DNAPL migration and remediation.

3.2 Results and discussion

3.2.1 PCE migration and its remediation based on single realizations

456   The simulation results of PCE migration for individual realization of porosity field for

457 RTA are shown in Fig. 5a-f. When PCE is released into aquifer into aquifer at the top layer of

458 spill position, PCE almost infiltrates vertically under the effect of gravity force (Fig. 5a). Due

459 to the heterogeneity of aquifer, some preferential flow appears and PCE plume becomes

460 irregular (Fig. 5b). After 30 days, PCE plume almost touches the bottom of aquifer (Fig. 5c).

461 When the PCE leakage is stopped, PCE continues to migrates continuouslyfreely in aquifer

462 for 70 days (Fig. 5d-f). The released PCE is migrating downward and entrapped by capillary

463 forces as residual ganglia and globules. Heterogeneity of aquifer makes PCE migrate along

464 preferential pathway. When PCE plume touches the zones of low permeability and high entry

465 pressure, it will bypass these zones and migrate continuously, which leads to an increasing

466 variability in PCE distribution. After PCE plume reaches the bottom of aquifer, PCE begins

467 accumulate and form contaminant pool at the bottom. At t=100 days, ~~A~~ a PCE pool is~~has been~~

468 formed at the bottom of aquifer, moving toward the right boundary.

469   Figs. 6a-f show the simulated PCE saturation for individual realization of porous media

470 for SPA during migration period. Under the effects of gravity force and natural hydraulic

471 gradient, PCE is migrating and ~~spreading~~ contaminant plume becomes larger and larger.

472 Heterogeneity of aquifer significantly changes the migration paths and leads to irregular

473 morphology of the PCE plume (Figs. 6a-c). However, due to the different micro-arrangement

474 of aquifer, the entry pressure ~~field~~ distribution also is different which leads to some

475 differences. After the PCE injection, the simulated PCE saturation in Figs. 6d-f indicates that

476 further trapping and spreading of the PCE occurs during this period. Compared with the

477 simulation results of RTA in Fig. 5, the PCE plume slightly seems similar in Fig. 6. Moreover,

478 PCE infiltrate more quickly in porous media of RTA in Fig. 5. After 70 days, PCE plume has

479 touched the bottom for RTA (Fig. 5e), while PCE plume based on SPA still keeps a significant

480 distance from bottom (Fig. 6e).

481   To clean up the DNAPL, 4% surfactant solution is injected through two injection wells

482 at a constant rate of 80 m^3/day over 50 days ~~to evaluate the effectiveness of surfactant~~

483 ~~flushing~~. Afterwards, following water-flush is applied during 150~300 day. The locations of

484 injection ~~wells~~ and production wells are presented in Fig. 3b. The production well is rightly

485 installed at the location of the PCE spill position and two injection wells are located 39 m

486 to the left and right of the production well. Figs. 5g-l shows the PCE remediation results of

487　individual realization for RTA. During the early remediation period, the effect of cleaning

488　up DNAPL is not yet apparent (Figs. 5g-i). When the water flushing begins, the surfactant

489　solution circulates throughout the contaminated aquifer (Figs. 5j-l). At t=200 days, ~~there~~

490　~~has been~~ 237.01 m^3 PCE ~~removal~~ is removed from contaminated aquifer, occupying

491　79.00% of the total released PCE (Fig. 5j). As time goes on, 268.30 m^3 PCE is removed

492　from aquifer and remediation efficiency reaches 89.43%.

493　　The same surfactant remediation is also conducted for individual realization ~~of~~

494　~~porous media for~~ SPA. Compare with the remediation for RTA, the remediation effect is

495　more apparent for SPA (Figs. 6g-l). As the remediation processes, more DNAPL is removed

496　and less DNAPL is remained ~~as small contaminant pools~~ at the bottom of aquifer. At t=200

497　day, 267.68 m^3 PCE is removed from contaminated aquifer~~,~~ and corresponding

498　remediation efficiency rise to 89.23%. At t=300 day, 285.32 m^3 PCE is cleaned up and

499　remediation efficiency reaches 95.11%. From results of remediation, it is obvious that

500　microstructure has effect on remediation ~~of~~for macroscopic scale aquifer. Results suggest

501　contaminated aquifer of RTA is hard to clean up by surfactant remediation while SPA can

502　improve DNAPL remediation efficiency.

3.2.2 PCE migration and SGS realizations

504　　PCE migration and remediation processes are simulated for 200 realizations of

505　porosity field for porous media of RTA and SPA. The variations of contaminant mass, the

506　ganglia-to-pool ratio (GTP) and moments of PCE plume versus time are presented in Figs.

507　7a-h. During 0~30 day, the PCE in aquifer increases linearly at a constant rate of 10 m^3/day

508　(Fig. 7a), which corresponding to contaminant spill stage. Afterward, PCE volume keeps

509 constant during the second stage ranged 30~100 day, while PCE volume in aquifer is

510 reduced when surfactant is injected into aquifer. After surfactant and water flushing the

511 contaminated aquifer, most DNAPL is cleaned up. The residual DNAPL mass remained in

512 aquifer of 0.67 m^3-119.89 m^3 with a mean of 22.42 m^3 and 0.79 m^3-103.33 m^3 with a mean

513 of 12.51 m^3 are achieve for 200 individual heterogeneous realizations based on the RTA and

514 SPA, respectively. The average remediation efficiency of SPA is undoubtedly higher than RTA,

515 indicating the aquifer of SPA is easier to clean up. PCE plume architectures are quantified by

516 measuring the ganglia-to-pool ratio (GTP) in Fig. 7b. Over entire periods, curves of GTP value

517 appear obvious oscillations. Surfactant has the ability of promoting solubilization and

518 mobilization of DNAPL can reduce GTP value. As a result, when surfactant is injected at

519 t=100 day, the GTP value reduces quickly. When surfactant injection is end and water flushing

520 begins, the GTP value increases with steep flank slope. At last, GTP values reach 0.10-0.41

521 with a mean of 0.21 and 0.15-0.42 with a mean of 0.28 for 200 individual heterogeneous

522 realizations based on the RTA and SPA, respectively.

523 Fig. 7c shows cumulative PCE removal from contaminated aquifer versus flushing time

524 for RTA and SPA. During the surfactant injection period ranged 100~150 day, the DNAPL

525 removal is not apparent, However, DNAPL is removed effectively and quickly during water

526 flushing period. Through long time remediation, the removal PCE from contaminated aquifer

527 reach 179.89 m^3-298.98 m^3 with a mean of 277.29 m^3 and 196.45 m^3-298.87 m^3 with a mean of

528 287.21 m^3 for 200 realizations based on RTA and SPA, respectively. Average remediation

529 efficiency of SPA (95.83%) is obvious higher than average remediation efficiency of RTA

530 (92.52%).

531   Fig. 7d shows the GTP value as a function of cumulative PCE removal for contaminated

532   aquifer. The GTP remains at a relatively low level before 30% of the DNAPL is removed from

533   aquifer. When 40% of the total 300 m^3 PCE are removed, GTP values are increasing and

534   corresponding curves appear a wave crest because the high saturation zone of PCE plume are

535   dissolved and turned into ganglia state. After the wave crest, the GTP values decline quickly

536   with steep flank slope due to PCE ganglia removal through water flushing. At last, GTP values

537   increase at the end of remediation process for 200 realizations, indicating most of PCE is

538   removed and most of residual PCE turn to ganglia state.

539   For the center of PCE plume in horizontal axis, associated variations versus time are

540   similar for 200 realizations based on RTA and SPA (Fig. 7e). Significantly, the PCE plume

541   vertical infiltration rate in aquifer of RTA is slightly faster than PCE infiltration in aquifer of

542   SPA for 200 realizations (Fig. 7f). Simultaneously, the second PCE plume moments in

543   horizontal direction of RTA are different from the second PCE plume moments in horizontal

544   direction of SPA (Fig. 7g). After PCE migration at natural condition at t=100 day, the second

545   PCE plume moments in horizontal direction are 10.61 m^2-40.50 m^2 with a mean of 21.51 m^2

546   and 10.99 m^2-36.38 m^2 with a mean of 20.75 m^2 for 200 realizations based on RTA and SPA,

547   respectively. At t=300 day, the second PCE plume moments in horizontal direction change to

548   0.81 m^2-34.88 m^2 with a mean of 5.79 m^2 and 1.03 m^2-24.57 m^2 with a mean of 4.64 m^2 for

549   RTA and SPA, respectively. The horizontal second moment of RTA is always larger than

550   horizontal second moment of SPA, indicating the PCE plume in aquifer of RTA is wider than

551   PCE plume in aquifer of SPA and RTA can cause larger range of groundwater contamination.

552   Similarly, the second moments in vertical direction offor RTA are larger than the second

553   moments in vertical direction ~~of~~for SPA.

554   This study takes an important step toward exploring how micro-scale arrangements

555   control contaminant migration at small aquifer scale. Results are essential to the macroscopic

556   aquifer composed of porous media without large heterogeneity, such as sandy aquifers

557   containing rich groundwater resources. However, upscaling problem of aquifer is widely

558   existed in nature (Dagan et al., 2013; Pacheco, 2013; Pacheco et al., 2015). Due to large

559   heterogeneity of natural aquifers, research results may be very different and can't be

560   extrapolated to complex regional aquifer at large scale. On the other hand, the finding in this

561   study is absolutely applicable for natural aquifers with similar heterogeneities. If the

562   heterogeneity and anisotropy of natural aquifers are very different, the effect of the micro-scale

563   arrangements on the macroscopic contaminant migration and remediation will be different.

564   Even realistic conditions are complex, the new findings achieved from this research also is

565   very significant for understanding the effect of micro-scale arrangements~~' effect~~ on

566   contaminant behaviors at aquifer scale. The upscaling problem of the results obtained at the

567   simulation scale (100 x 25 x 25 m) is the basis and the upscaling problem with more complex

568   heterogeneity conditions is needed to be further investigated. Various researches on upscaling

569   problem are done from the aspects of experiment and simulation (Wu et al., 2017a, 2017b,

570   2017c, 2017d). Based on these research, the microstructure of porous media is developed and

571   the contaminates migration in porous media are explored using fractal methods in this study,

572   implying the experimental results are very significant for realistic problems at aquifer scale.

573   Our next procedure is applying these models in realistic aquifer with complex heterogeneity

574   conditions and modifying our models and method according to realistic conditions.

4. Conclusions

The micro-structure of aquifer has important effect on macroscopic scale characteristics of ~~aquifer and inner~~ contaminant migration and remediation. In this study, we focus on the DNAPL migration and remediation in heterogeneous aquifers composed of granular porous media with RTA and SPA. The microscale models of RTA and SPA are developed to obtain the mathematical expressions of permeability and entry pressure using fractal method. 200 realizations of porosity field are generated using SGS method and PCE is released from underground storage tank into heterogeneous aquifer. To clean up contamination caused by underground storage tank spill, surfactant remediation technique is used to remove contaminants in aquifer. The entire process of DNAPL migration and remediation is simulated by a multicomponent, multiphase model simulator UTCHEM. Results suggest RTA not only cause larger range of groundwater contamination than RTA, but also the contaminated aquifer of RTA is harder to clean up compared with SPA. The second PCE plume moments in horizontal direction are 10.61 m^2-40.50 m^2 with a mean of 21.51 m^2 and 10.98 m^2-36.38 m^2 with a mean of 20.75 m^2 for 200 realizations based on RTA and SPA after ~~PCE natural~~ long-term migration at t=100 day, respectively. Furthermore, the second PCE plume moments in horizontal direction at t=300 day are 0.807 m^2-34.88 m^2 with a mean of 5.79 m^2 and 1.025 m^2-24.57 m^2 with a mean of 4.64 m^2 for RTA and SPA respectively after ~~long time~~ long-term remediation. Simultaneously, the residual DNAPL mass remained in aquifer are 0.67 m^3-119.89 m^3 with a mean of 22.42 m^3 and 0.79 m^3-103.33 m^3 with a mean of 12.51 m^3 for RTA and SPA respectively, indicating remediation efficiency of SPA (65.53%-99.74% with a mean of 95.83%) mostly is higher than remediation efficiency of RTA (60.01%-99.78% with a

mean of 92.52%). This study ~~proves~~ reveals the microstructure of aquifer has important effect on contaminant movement and associated remediation efficiency ~~in~~ at macroscopic scale ~~aquifer~~, which is very essential and significant for dealing with the accidental event of underground storage tank spill and identifying subsurface contaminant source in the future.

Acknowledgments

References

Ahn, K.J., Seferis, J.C.: Simultaneous measurements of permeability and capillary pressure of thermosetting matrices in woven fabric reinforcements, Polym. Composite., 12, 146-152, 1991.

An, C.J., McBean, E., Huang, G.H., Yao, Y., Zhang, P., Chen, X.J., Li, Y.P.: Multi-Soil-Layering Systems for Wastewater Treatment in Small and Remote Communities, J. Environ. Inform., 27(2), 131-144, 2016.

Bakshevskaia, V.A., Pozdniakov, S.P., Simulation of hydraulic heterogeneity and upscaling permeability and dispersivity in Sandy-Clay foormations, Math. Geosci., 48, 45-64, 2016.

619 Bear, J.: Dynamics of fluids in porous media, Dover, New York, 1972.

620 Bob, M.M., Brooks, M.C., Mravik, S.C., Wood, A.L.: A modified light transmission

621   visualization method for DNAPL saturation measurements in 2-D models, Adv. Water

622   Resour., 31, 727-742, 2008.

623 Boswinkel, J.A.: International Groundwater Resources Assessment Centre (IGRAC),

624   Netherland Institute of Applied Geoscience, Netherlands, 2000.

625 Cui, Q.L., Wu, H.N., Shen, S.L., Yin, Z.Y., Horpibulsuk, S.: Protection of neighbour buildings

626   due to construction of shield tunnel in mixed ground with sand over weathered granite,

627   Environ, Earth Sci., 75, 458, 2016.

628 C.Carroll, K., McDonald, K., Marble, J., Russo, A.E., Brusseau, M.L.: The impact of

629   transitions between two-fluid and three-fluid phases on fluid configuration and fluid-fluid

630   interfacial area in porous media, Water Resour. Res., 51, 7189-7201, 2015.

631 Dagan, G., Fiori, A., Jankovic, I.: Upscaling of flow in heterogeneous porous formations:

632   Critical examination and issues of principle, Adv. Water Resour., 51, 67-85, 2013.

633 Dawson, H.E., Roberts, P.V.: Influence of Viscous, Gravitational, and Capillary Forces on

634   DNAPL Saturation, Groundwater, 35(2), 261-269, 1997.

635 Delshad, M., Pope, G.A., Sepehrnoori, K.: A compositional simulator for modeling surfactant

636   enhanced aquifer remediation, 1 Formation, J. Contam. Hydrol., 23, 303-327, 1996.

637 Eggleston, J.R., Rojstaczer, S.A., Peirce, J.J.: Identification of hydraulic conductivity structure

638   in sand and gravel aquifers: Cape Cod data set, Water Resour. Res., 32, 1209–1222,

639   1996.

640 Essaid, H.I., Bekins, B.A., Cozzarelli, I.M., Organic contaminant transport and fate in the

641   subsurface: Evolution of knowledge and understanding, Water Resour. Res., 51,

642   4861-4902, 2015.

643   Feng, Y.J., Yu, B.M.: Fractal dimension for tortuous streamtubes in porous media, Fractals, 15,

644   385-390, 2007.

645   Hadley, P.W., Newell, C.: The New Potential for Understanding Groundwater Contaminant

646   Transport, Groundwater, 52(2), 174-186, 2014.

647   Hu, K., White, R., Chen, D., Li, B., Li, W.: Stochastic simulation of water drainage at the field

648   scale and its application to irrigation management, Agr. Water Manage., 89, 123-130,

649   2007.

650   Huang, J.Q., Christ, J.A., Goltz, M.N., Demond, A.H.:   Modeling NAPL dissolution from

651   pendular rings in idealized porous media, Water Resour. Res., 51, 8182-8197, 2015.

652   Katz, A.J., Thompson, A.H.: Fractal sandstone: Implications for conductivity and pore

653   formation, Phys. Rev. Lett., 54,   325-332, 1985.

654   Krohn, C.E.: Sandstone fractal and Euclidean pore volume distributions, J. Geophys. Res., 93,

655   3286-3296, 1988.

656   Liang, C., Hsieh, C.L.: Evaluation of surfactant flushing for remediating EDC-tar

657   contamination, J. Contam. Hydrol., 177-178, 158-166, 2015.

658   Liang, C., Lai, M.C.: Trichloroethylene degradation by zero valent iron activated persulfate

659   oxidation, Envrion. Eng. Sci., 25(7), 1071-1077, 2008.

660   Liu, H., Li, Y.X., He, X., Sissou, Z., Tong, L., Yarnes, C., Huang, X.: Compound-specific

661   carbon isotopic fractionation during transport of phthalate esters in sandy aquifer,

662   Chemosphere, 144, 1831-1836, 2016.

663   Liu, L.: Modeling for surfactant-enhanced groundwater remediation processes at

DNAPLs-contaminated sites, J. Environ. Inform., 5(2), 42-52, 2005.

Liu, L., Hao, R.X., Cheng, S.Y.: A possibilistic analysis approach for assessing environmental

risks from drinking groundwater at petroleum-contaminated sites, J. Environ. Inform.,

2(1), 31-37, 2003.

Liu, Y., Wang, S., McDonough, C.A., Khairy, M., Muir, D.C.G., Helm, P.A., Lohmann, R.:

Gaseous and freely-dissolved PCBs in the lower great lake based on passive sampling:

spatial trends and air-water exchange, Environ. Sci. Technol., 50, 4932-4939, 2016.

Mishra, A.K., Kumar, B., Dutta, J.: Prediction of hydraulic conductivity of soil bentonite

mixture using Hybrid-ANN approach, J. Environ. Inform., 27(2), 98-105, 2016.

Pacheco, F.A.L.: Hydraulic diffusivity and macrodispersivity calculations embedded in a

geographic information system, Hydrolog. Sci. J., 58(4), 930-943, 2013.

Pacheco, F.A.L., Landim, P.M.B., Szocs, T.: Bridging hydraulic diffusivity from aquifer to

particle-size scale: a study on loess sediments from southwest Hungary, Hydrolog. Sci.

J., 60(2), 269-284, 2015.

Pfeifer, P., Avnir, D.: Chemistry in Nonintegral dimensions between two and three. I . Fractal

theory of heterogeneous surface, J. Chem. Phys., 79, 3558-3565, 1983.

Qin, X.S., Huang, G.H., Chakma, A., Chen, B., Zeng, G.M.: Simulation-based process

optimization for surfactant-enhanced aquifer remediation at heterogeneous

DNAPL-contaminated sites, Sci. Total Environ., 381, 17-37, 2007.

Schaefer, C.E., White, E.B., Lavorgna, G.M., Annable, M.D.:   Dense nonaqueous-phase liquid

architecture in fractured bedrock: implications for treatment and plume longevity,

Environ. Sci. Technol., 50, 207-213, 2016.

Shen, J., Huang, G., An, C.J., Zhao, S., Rosendahl, S.: Immobilization of tetrabromobisphenol

A by pinecone-derived biochars at solid-liquid interface Synchrotron-assisted analysis

and role of inorganic fertilizer ions, Chen. Eng. J., 321, 346-357, 2017.

Valipour, M.: Comparison of surface irrigation simulation models: Full hydrodynamic, zero

inertia, kinematic wave, J. Agr. Sci., 4(12), 68-74, 2012.

Valipour, M.: Future of agricultural water management in Africa, Arch, Agron. Soil Sci., 61(7),

907-927, 2015.

Valipour, M., Singh, V.P.: Global experiences on wastewater irrigation: challenges and

Prospects, in: Maheshwari, B., Singh, V.P., Thoradeniya, B., Balanced urban

development: options and strategies for liveable cities, Volume 72 of the series Water

Science and Technology Library, pp. 289-327, 2016.

Veneziano, D., Tabaei, A.: Nonlinear spectral analysis of flow through porous media with

isotropic lognormal hydraulic conductivity, J. Hydrol., 294, 4-17, 2004.

Weathers, T.S., Harding-Marjanovic, K., Higgins, C.P., Alvarez-Cohen, L., Sharp, J.O.:

Perfluoroalkyl acids inhibit reductive dechlorination of Trichloroethene by repressing

dehalococcoides, Environ. Sci. Technol., 50, 240-248, 2016.

Wu, M., Cheng, Z., Wu, J.F., Wu, J.C.: Quantifying representative elementary volume of

connectivity for translucent granular materials by light transmission micro-tomography,

J. Hydrol., 545, 12-27, 2017a..

Wu, M., Cheng, Z., Wu, J.F., Wu, J.C.: Estimation of representative elementary volume for

DNAPL saturation and DNAPL-water interfacial areas in 2D heterogeneous porous

media, J. Hydrol., 549, 12-26, 2017b.

Wu, M., Wu, J.F., Wu, J.C.: Simulation of DNAPL migration in heterogeneous translucent

porous media based on estimation of representative elementary volume, J. Hydrol.,

553, 276-288, 2017c.

711   Wu, M., Cheng, Z., Wu, J.F., Wu., J.C.: Precise simulation of long-term DNAPL migration in

712   heterogeneous porous media based on light transmission micro-tomography, J. Environ.

713   Chem. Eng. 5, 725-734, 2017d.

714   Yannopoulos, S.I., Lyberatos, G., Theodossiou, N., Li, W., Valipour, M., Tamburrino, A.,

715   Angelakis, A.N.: Evolution of water lifting devices (pumps) over the centuries

716   worldwide, Water, 7, 5031-5060, 2015.

717   Yu, B.M.: Fractal character for tortuous streamtubes in porous media, CHIN. PHYS. LETT., 22,

718   158-160, 2005.

719   Yu, B.M., Cai, J.C., Zou, M.Q.: On the physical properties of apparent two-phase fractal

720   porous media, Vadose Zone J., 8, 177-186, 2009.

721   Yu, B.M., Cheng, P.: Fractal models for the effective thermal conductivity of bidispersed

722   porous media, J. Thermophys. Heat Tr., 16, 22-29, 2002.

723   Yu, B.M., Li, J.H.: A geometry model for tortuosity of flow path in porous media, CHIN.

724   PHYS. LETT., 21, 1569-1571, 2004.

725   Yun, M.J., Yu, B.M., Zhang, B., Huang, M.T.: A geometry model for tortuosity of streamtubes

726   in porous media with spherical particles, CHIN. PHYS. LETT., 22(6), 1464-1467,

727   2005.

728

729 **Table 1.** Parameters used in simulation

Parameter	Value
Average value of porosity	0.22
Standard deviation of porosity	0.06
Longitudinal dispersivity	1.0 m
Transverse dispersivity	0.1 m
Hydraulic gradient	0.005 m/m
Water density	1.00 g/cm^3
PCE density	1.63 g/cm^3
Surfactant density	1.15 g/cm^3
Water viscosity	1.00 cp
PCE viscosity	0.89 cp
PCE/ Water interfacial tension	45 dyn/cm
PCE solubility in water	240 mg/L
Residual water saturation	0.24
Residual PCE saturation	0.17
Endpoint of Water (BC model)	0.486
Endpoint of PCE (BC model)	0.65
Exponent of Water (BC model)	2.85
Exponent of PCE (BC model)	2.7
Exponent of capillary pressure	-0.52

730

731

732 **Figure Captions**

733

734 **Figure 1.** Two different microscale arrangements of solid particles: (a) RTA; and (b) SPA

735 **Figure 2.** Three kinds of Sierpinkski gasket [30]: (a) L_a=2; (b) L_a=3; and (c) L_a=5

736 **Figure 3.** (a) Two-dimensional view of contaminated domain; and (b) locations of injection

737   and extraction wells

738 **Figure 4.** (a) The individual porosity field generated by Sequential Gaussian Simulation (SGS)

739   method; (b) the frequency of individual porosity field; (c) the individual permeability

740   field of RTA obtained from individual porosity field; (d) the frequency of individual

741   permeability field for RTA; (e) the individual permeability field of SPA obtained from

742   individual porosity field; (f) the frequency of individual permeability field for SPA; (g)

743   The obtained individual entry pressure field of RTA; (h) the frequency of individual

744   entry pressure field of RTA; (i) the obtained individual entry pressure field of SPA;

745   and (j) the frequency of individual entry pressure of SPA

746 **Figure 5.** Simulated PCE saturation for individual realization of RTA over the entire

747   migration and remediation periods (0~300 day)

748 **Figure 6.** Simulated PCE saturation for individual realization of SPA over the entire

749   migration and remediation periods (0~300 day)

750 **Figure 7.** (a) PCE volume in aquifer versus time, RTA represents RTA and SPA represents

751   SPA; (b) Changes in GTP as a function of time; (c) Cumulative DNAPL removal as a

752   function of time; (d) Variation of GTP value as a function of cumulative DNAPL

753   removal percent; (e) the change of the center of PCE plume during the entire periods

754   of migration and remediation; (f) the change of the depth of PCE plume center during

755   the entire periods; (g) variation of second PCE plume moment in horizontal axis; and
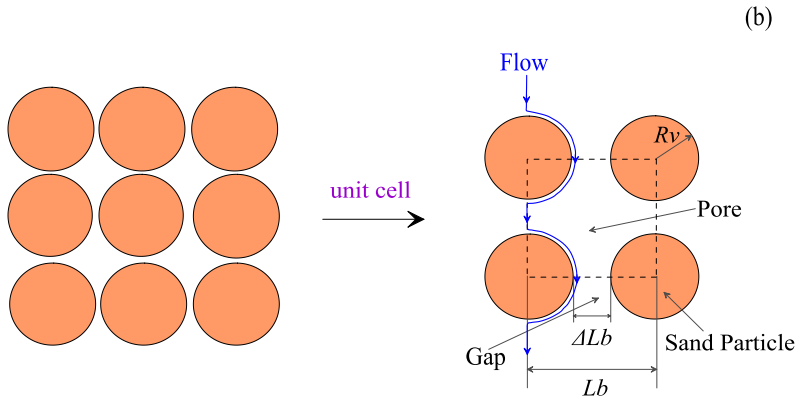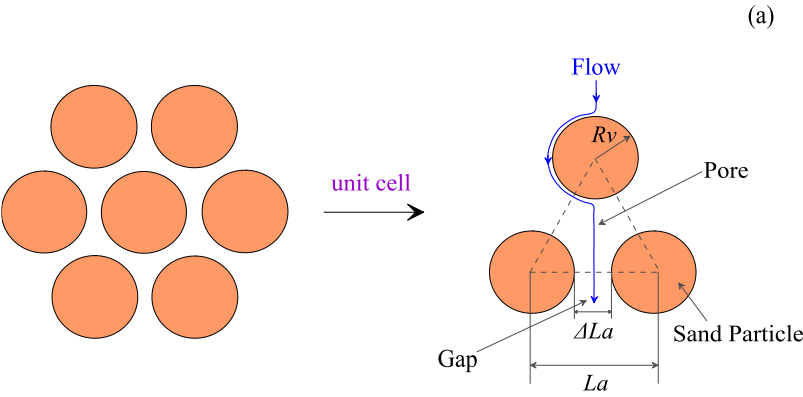
756   (h) variation of second PCE plume moment in vertical axis
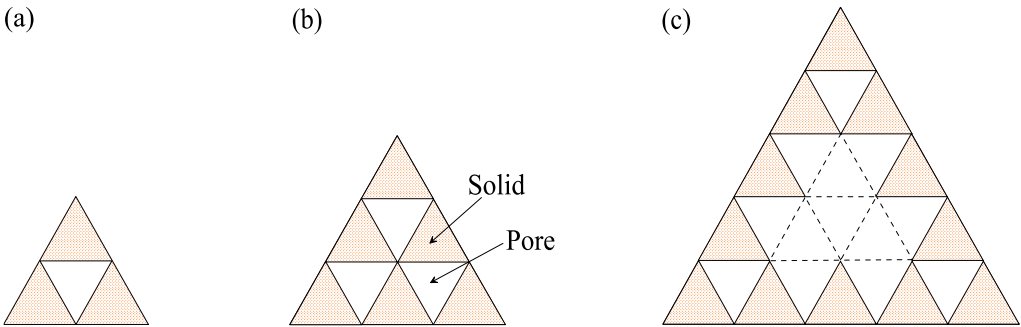
757

758

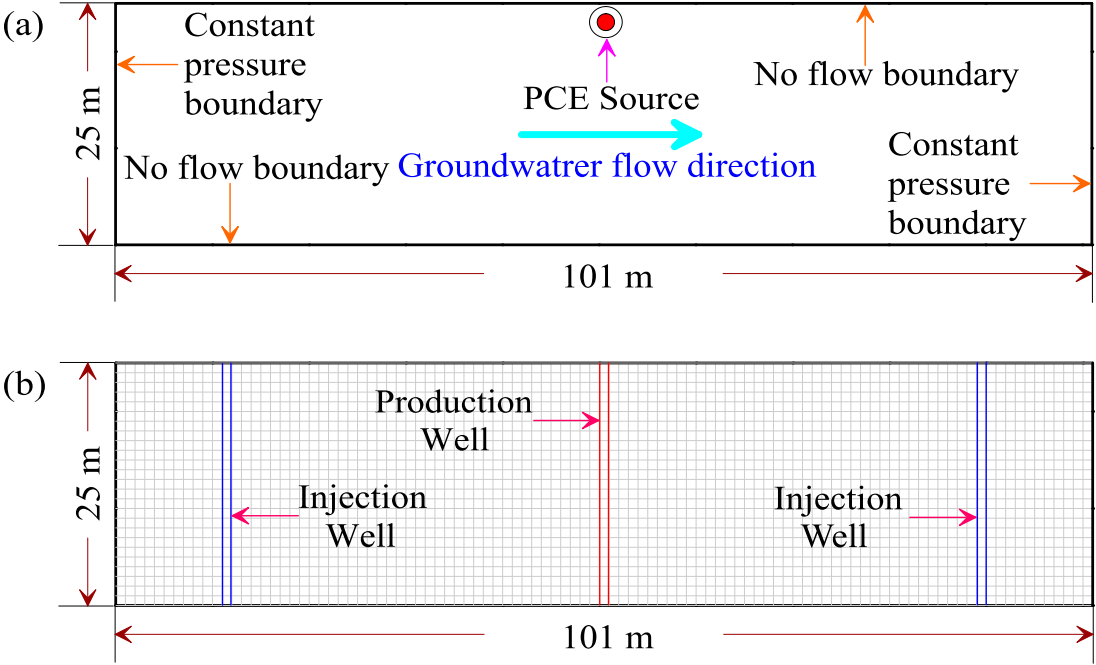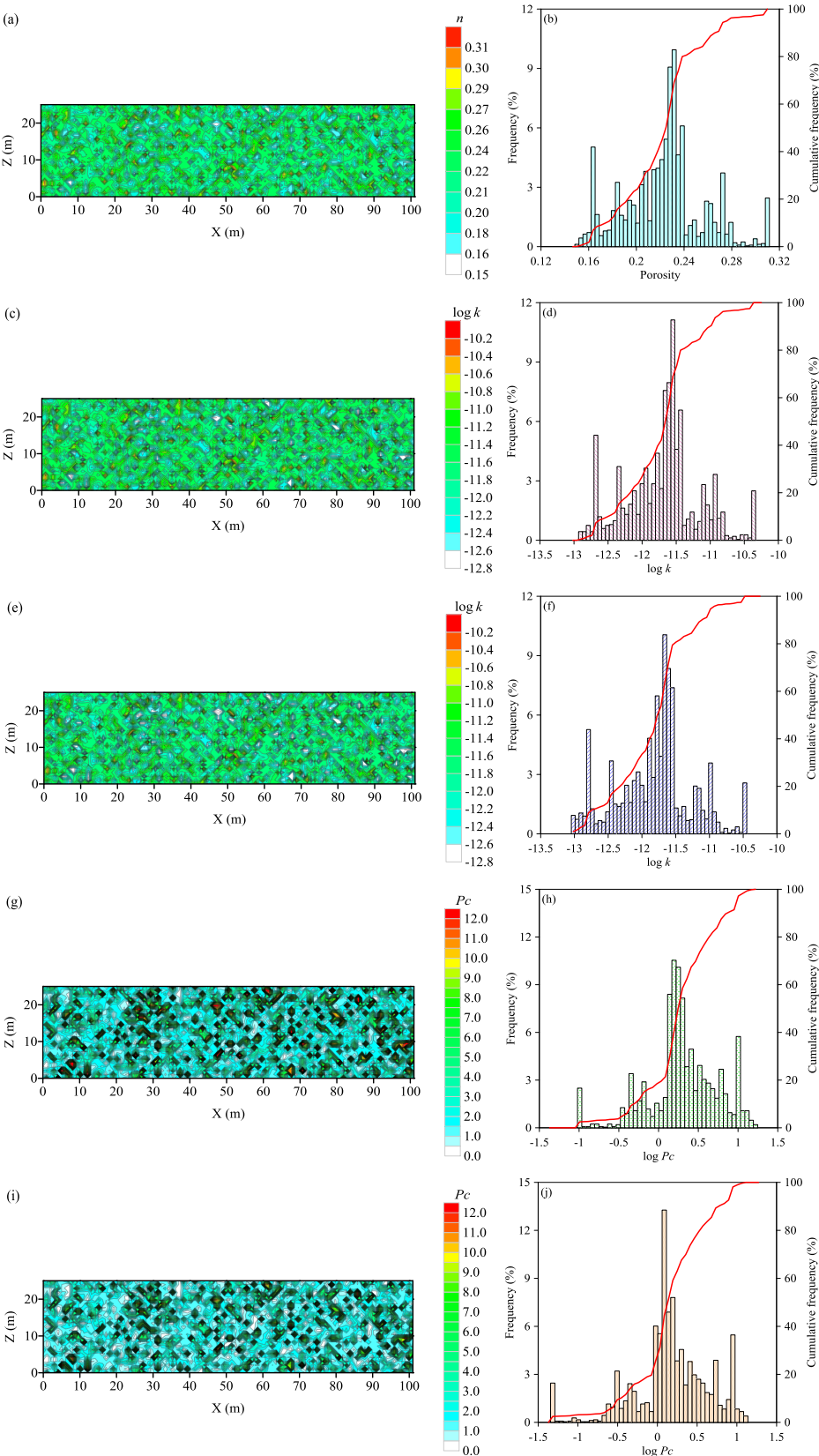759 **Figure 1**

760

761

762

763   **Figure 2**

764

(a)   (b)   (c)

Solid

Pore

765

766

767

768 **Figure 3**

769

(a) 25 m, 101 m — Constant pressure boundary, No flow boundary, PCE Source, Groundwatrer flow direction, No flow boundary, Constant pressure boundary

(b) 25 m, 101 m — Production Well, Injection Well, Injection Well

770

771

772   **Figure 4**

773

774

775

776

777

778

779

Figure 5

784   **Figure 6**

785

786

787

788   **Figure 7**

789

790
791